ADVANCED OPTICAL MATERIALS
www.advopticalmat.de

Bio-Engineering Yeast Cells Biolenses by Reshaping Intracellular Vacuoles

Daniele Pirone, Massimo D'Agostino, Matteo Lombini, Fausto Cortecchia, Emiliano Diolaiti, Giuseppe Mongelluzzo, Giusy Giugliano, Vittorio Bianco, Lisa Miccio, Pasquale Memmolo,* and Pietro Ferraro*

An intriguing field of research has recently emerged in which biological cells can be demonstrated to behave as photonics devices, such as optical microlenses. This research highlights yeast cells as promising candidates for engineering biolenses with customizable focal properties. Typically serving as positive biolenses due to their quasi-spherical shape and positive refractive index (RI) contrast, yeast cells can achieve a negative lensing effect by manipulating their intracellular content, without altering their overall morphology. In fact, it shows that exposure to hypotonic conditions induces the formation of a large, roundish vacuole with lower RI values with respect to the surrounding cytoplasm, thus altering the cell's optical properties. This behavior is investigated by using 3D RI tomograms obtained through a holo-tomographic phase imaging flow cytometry system, demonstrating that the anisotropic nature of yeast cells results in focal properties dependent on their specific orientations in respect to the incident light. Furthermore, Zemax OpticStudio is utilized to perform comprehensive assessments for optical design analysis of the obtained cell biolenses. The methods described here and the related results represent a pioneering investigation of biological cells' metamorphoses via intracellular content manipulation for biolens applications.

1. Introduction

The possibility of using a live cell as a photonics/optics component is fascinating and somehow visionary since it could open completely new scenarios in the future biotechnology field. It has been demonstrated that, in proper conditions, living cells perform as microlenses, resonators, waveguides, optical tweezers, or gratings and, also, as gain medium for optical laser cavities.[1] In particular, by modeling a single cell as a microlens, it is possible to exploit all optical and computational tools to characterize such lens, in analogy to indirect adaptive optics.[2] The first demonstration that a biological cell can act as an optical lens was given in 2015 by using red blood cells (RBCs).[3] The two main parameters that affect the behavior of a microlens are the lens' shape and its refractive index (RI).[4] For example, as healthy RBCs have a flexible biconcave shape with an almost homogeneous RI distribution, they were modeled as disk-shaped microlenses with a quasi-constant RI.[3] Therefore, it was possible to characterize RBCs as microlenses with aberrations identifying focal properties and morphological deviations from normal shapes by using well-established optical testing methods based on Zernike analysis.[3,5,6]

Later on, many groups carried out remarkable research activities where live biolenses can operate as real-world optical components.[4] For instance, since RBCs can behave as tunable liquid lenses by changing the chemical buffer, it is possible to control the focal properties and the corresponding imaging properties, thus performing a preliminary screening and sorting between discocytes and spherocytes for diagnostic purposes.[3] The same properties have been explored for producing efficient photonics nanojets that could be used as optical tweezers.[7] Optical properties of single cells have been used to measure the real-time chemical efflux of cell populations,[8,9] while a random optical probing based on Fourier Ptychographic Microscopy was demonstrated.[10] Under specific circumstances, the collective effect of RBCs can produce non-diffractive effects[11] or reveal the formation of rough waves.[12] Regarding imaging, it was also proved that arrays of self-assembled RBCs show self-imaging or

D. Pirone, G. Giugliano, V. Bianco, L. Miccio, P. Memmolo, P. Ferraro
CNR-ISASI
Istituto di Scienze Applicate e Sistemi Intelligenti "E. Caianiello"
Via Campi Flegrei 34, Pozzuoli, Napoli 80078, Italy
E-mail: daniele.pirone@isasi.cnr.it; pasquale.memmolo@isasi.cnr.it
M. D'Agostino
DMMBM
Dipartimento di Medicina Molecolare e Biotecnologie Mediche
University of Naples "Federico II"
Via S. Pansini 5, Napoli 80131, Italy
M. Lombini, F. Cortecchia, E. Diolaiti
INAF
Istituto Nazionale di Astrofisica – Osservatorio di Astrofisica e Scienza dello Spazio di Bologna
Via Gobetti 93/3, Bologna 40129, Italy
G. Mongelluzzo
INAF
Istituto Nazionale di Astrofisica – Osservatorio Astronomico di Capodimonte
Salita Moiariello 16, Napoli 80131, Italy

The ORCID identification number(s) for the author(s) of this article can be found under https://doi.org/10.1002/adom.202400164

DOI: 10.1002/adom.202400164

Talbot effect.[13] Super-resolution imaging was obtained by exploiting living cells as biolenses in optical devices.[14,15] as well as intracellular organelles like lipid droplets (LDs).[16] Another recent application regards the detection of cells exhibiting large and numerous LDs based on their biolens signature, which is helpful for diagnostic purposes.[17]

When a single live cell is imaged in suspension, its usual behavior from the optical point of view is essentially that of a positive (i.e., convergent) optical lens.[18] Indeed, the main body of the suspended cell, which has a quasi-spherical shape, is embedded in a typical water-based liquid medium with a lower RI. For this reason, the effect of a negative (i.e., divergent) optical lens, limited to the paraxial rays, has been observed in RBCs with non-spherical shapes such as discocytes, which were converted into positive optical lenses by changing the chemical buffer to create a quasi-spherical shape (i.e., spherocytes).[3] Instead, negative focal effects for single quasi-spherical biolenses have never been observed so far.

Without changing the overall cell's shape, here we propose to alter the intracellular content at the aim to convert a quasi-spherical cell from a purely convergent lens into an optical system with additional divergent properties. To demonstrate this concept, we use yeast cells as a model because of the possibility of quickly reshaping the intracellular vacuoles, thus creating one single large and roundish vacuole.[19] In fact, vacuoles generally have an average RI lower than the average RI of the hosting cell (i.e., a negative RI contrast),[20,21] therefore an additional quasi-spherical domain behaving as a negative optical lens is created inside the positive quasi-spherical biolens (i.e., the host cell). In order to measure the 3D RI distribution of the cells with vacuoles in suspension conditions, we employ a Tomographic Phase Imaging (TPI) system implemented in Flow Cytometry mode (namely, TPIFC technique), which is based on a digital holography (DH) microscope coupled to a flow-cytometry modulus to record flowing and rotating biological samples.[19,22,23] Then, the availability of 3D RI tomograms allows us to isolate the intracellular compartments, thus studying the focal properties of these single optical biolenses alone and their contribution to the overall optical system represented by the whole cell. In particular, the interferometric working principle of DH allows numerically propagating the complex wavefront modulated by the cell by means of a well-established method,[24] thus emulating the light propagation in a realistic way. Therefore, a DH-based method is employed to characterize the focal properties of the yeast cells recorded by means of the experimental TPIFC system. Then, a commercial software for the optical design (i.e., Zemax OpticStudio) is exploited to further assess the DH-based characterization by means of numerical simulations. Remarkably, the output of numerical simulations in Zemax OpticStudio were in good agreement with the well-established DH-based characterization of focal properties related to the experiment on yeast cells. Finally, thanks to the DH-based characterization of the TPIFC 3D experimental data, changes in the focal properties of the optical system of biolenses are evaluated with respect to the orientation of the incident light, and an example of a complex optical system made of positive-negative biolenses is reported.

Applications of biolenses for imaging have been demonstrated in literature at the aim to go beyond the diffraction limit,[7] and also the magnification capability of inner cell structures have been demonstrated for LDs by enhancing the fluorescent imaging of molecules.[16] Our findings reveal that modifying a distinct class of inner structures, such as cytoplasmic vacuoles, can alter the lensing behavior of cells. A key discovery of this study is the expansion of capabilities within the bio-lensing paradigm. Future applications may include integrating two or more inner structures to achieve super-resolution imaging or to correct for certain aberrations, just to mention a couple of possibilities. For example, the positive biolens effect of yeast cells has been already exploited for super-resolution purposes.[25] Possible future applications would integrate advanced optical technologies as optical tweezers to trap and move in 3D multiple cellular compartments to enhance fluorescence signaling. A further example would be mimicking fly's eyes arrays by exploiting an ensemble of vacuoles closely packaged. It can be envisaged that a set of vacuoles located externally on the spherical nucleus shape may mimic negative microlens array on a curved substrate to resolve organelles inside the nucleus.[26] Hence, the driving reasons to further develop the proposed approach stand in the inner biocompatibility of the biological microlenses and the no-need of multistep fabrication processes.

A further class of practice applications would concern diagnosis as the biolens description could allow to identify living cells and some of their inner structures by means of an all-optical fingerprint. Modifications in the morphologies or in the content of the cells translate into different optical properties. First demonstration of diagnostic applications has been described on RBCs.[3] The biolens signature has also been exploited to detect monocytes and ovarian cancer cells with large and numerous LDs in a DH flow cytometer.[17] Even if we provide this proof-of-concept study for model yeast cells, vacuoles are also formed in mammals under various pathological situations present in many cell lines. For example, TPI has been recently employed to study the association between vacuoles and cancer senescent engulfing cells.[27] In fact, vacuoles are often correlated to diseases, inflammations, and cell malfunctioning.[28,29] In particular, intracellular vacuolar structures have been described in the peripheral blood cells of patients affected by several genetic disorders belonging to the lysosomal storage diseases family (LSDs),[30] cancer,[31–35] and viral infections,[36–38] including the more recent SARS-CoV-2.[39] Vacuoles have also been found in the macrophages of patients exposed to the lipopolysaccharide (LPS) of Gram-negative bacteria.[40] In addition, vacuoles are also reported in leukocytes upon exposure to various chemicals.[41,42] Indeed, many drugs used for oncologic treatment are weak bases that can be protonated and sequestered within lysosomes, thereby causing their vacuolation,[43] and exerting chemoresistance in cancer cells.[44] The motivation to further investigate such new insight in bioimaging field is the complete label-free nature of the presented approach that is green, non-invasive, low-cost, and, in some cases, faster compared to biochemical assays currently used in biology and biomedicine.

2. Results and Discussion

With the aim to demonstrate that, under specific conditions, cells can also have a negative lens effect, we use the baker yeast Saccharomyces cerevisiae as a biological model.[45] Among several membrane-enclosed organelles that can be found inside the

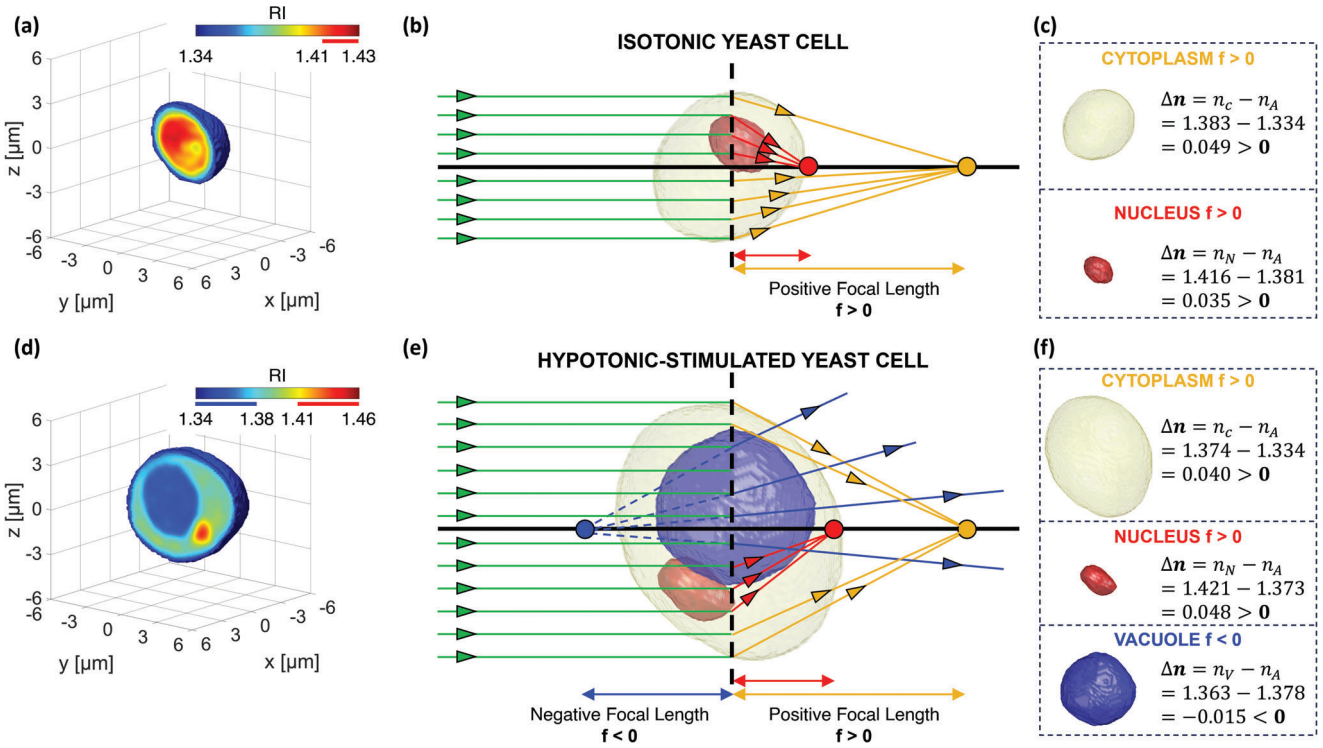

Figure 1. 3D RI tomograms of a (a-c) yeast iso-cell and a (d-f) yeast hypo-cell imaged by the TPIFC system. a,d) Central slice in which the vacuole has the lowest RIs (dark blue voxels in (d)) and the nucleus has the highest RIs (dark red voxels in (a,d)). b,e) Isolevels representation of the cytoplasm (yellow) along with the vacuole (blue) and the nucleus (red) segmented through the RI thresholding highlighted in the colorbars in (a,d), respectively. The cell illuminated by a parallel beam (green rays) can focus the light on the positive direction due to the cytoplasm (yellow rays) and the nucleus (red rays). In the hypotonic-stimulated yeast cell in (e), the cell can virtually focus the light also in the negative direction (blue rays) due to the large and roundish vacuole. c,f) The cytoplasm and the nucleus inside the cytoplasm have a positive focal length, while the vacuole inside the cytoplasm has a negative focal length, according to their RI contrast Δn reported on the right. n_c, n_N, and n_V are the average RI values of the cytoplasm, nucleus, and vacuole, respectively. n_A is the average RI of the ambiance, i.e., the surrounding medium in the cytoplasm case, the cytoplasm without the nucleus in the nucleus case, and the cytoplasm without the vacuole in the vacuole case.

cytoplasm, vacuoles are important catabolic sites,[46] whose morphology is highly dynamic and sensitive to the osmotic growth conditions. For instance, under hypertonic conditions, vacuole fragments become more numerous and smaller. On the contrary, under hypotonic conditions, vacuoles fuse together to form a single roundish larger vacuole.[47] Therefore, we exposed yeast cells to hypotonic stress by placing them in water for 10 min (see the Experimental Section). In the following, we will refer to the cells before and after water exposure as isotonic-cells (or iso-cells) and hypotonic-stimulated cells (or hypo-cells), respectively. Then, we imaged them using the TPIFC recording system and the corresponding holo-tomographic numerical processing described in the Methods section.[19] The central slices of the resulting 3D RI tomogram of an iso-cell and an hypo-cell are shown in **Figure** 1a,d, respectively. Since vacuoles have an aqueous content, their RI values are expected to be the lowest inside the cell.[20,21] In fact, in the hypo-cell in Figure 1d, a large roundish blue region with very low RIs can be clearly recognized, which is instead missing in the iso-cell in Figure 1a since the reshaping process of the multiple small vacuoles into one single large roundish vacuole has not been performed. For this reason, the vacuolar compartment can be easily segmented through a low RI threshold in the hypo-cell, as displayed in blue in the isolevels representation in Figure 1e. At the same time, in both the iso-cell and the hypo-cell in Figure 1a,d, their nuclei can be observed at the highest RI values,[19,21] since they contain most of the cellular genetic material, and thus they have been segmented again by a RI thresholding, as reported in red in Figure 1b,e, respectively. The histograms of the RI values related to the iso-cell in Figure 1a,b and the hypo-cell in Figure 1d,e are shown in Figure S1a,b (Supporting Information), respectively. By separating the contribution of the cytoplasm, nucleus, and vacuole, it can be seen that the RI histograms of the several cell components are mostly overlapped each other, meaning that there are no clear discontinuities among the RI values, which instead gradually change within the overall cell, as also visible in the central slices in Figure 1a,d.

In Figure 1b,e, a simplified sketch of a complex effect such as the cellular biolensing is reported, with the aim to highlight the main contributions to the positive and negative lensing effects. As sketched in Figure 1b,e, it is well known that, if the overall cell is illuminated by a parallel beam (parallel green rays), light is focused along the positive direction of the optical axis (convergent yellow and red rays).[18] However, in the following, we show that the presence of a large and roundish vacuole makes the hypo-cell a system of lenses able to focus the incident light both in the positive and negative directions of the optical axis (divergent blue

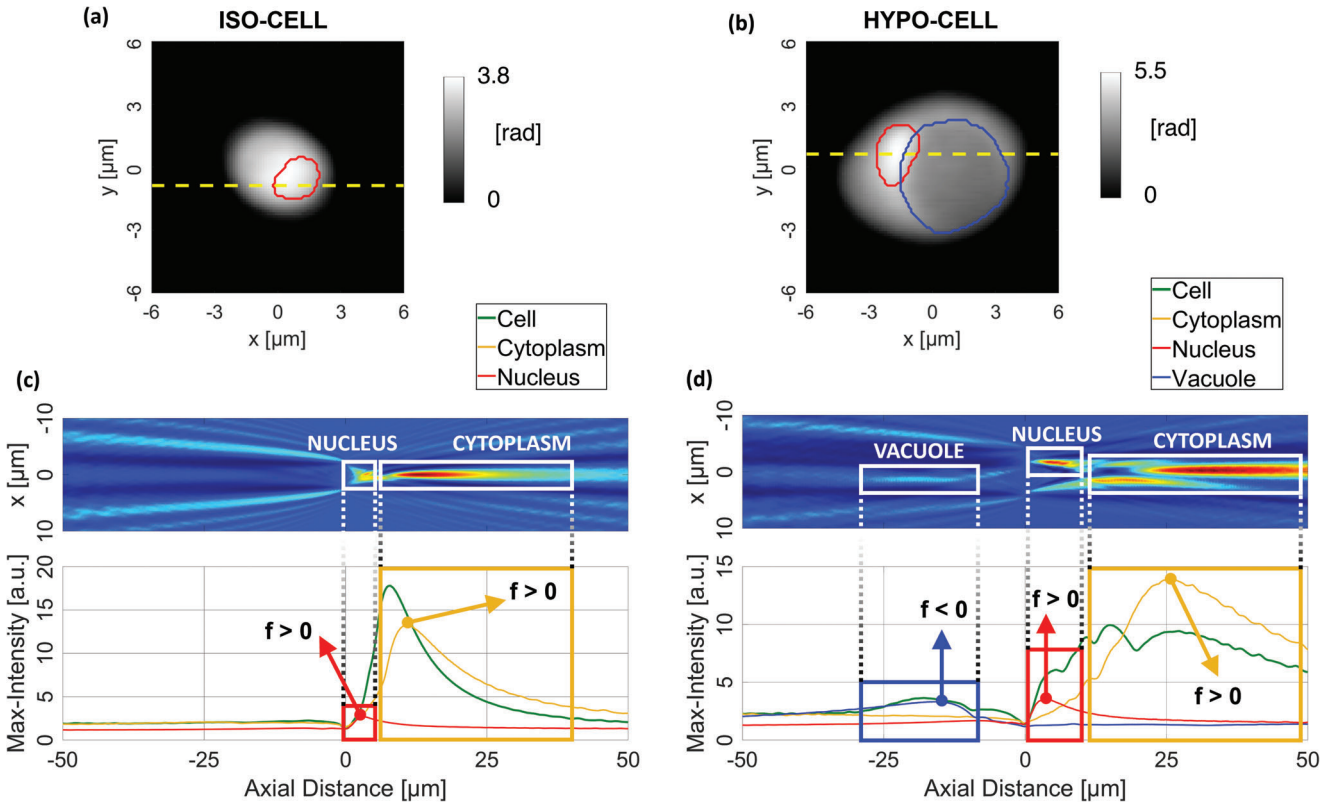

Figure 2. Focalization of a (a,c) yeast iso-cell and a (b,d) yeast hypo-cell obtained through the DH-based method (see Video S1, Supporting Information, with the whole axial scanning). a,b) QPM reprojected from the 3D RI tomogram through the IBPM, in which the contours of the nucleus and the vacuole are highlighted in red and blue, respectively. c,d) At the top, intensity profile made of the intensity values computed for each axial distance along the yellow line in (a,c), respectively. At the bottom, max-intensity curve of the overall cell (green), the sole cytoplasm (yellow), the sole nucleus (red), and the sole vacuole (blue). Focal regions of the cytoplasm, nucleus, and vacuole are highlighted in the boxes. Arrows indicate focal planes.

rays in Figure 1e). In particular, we show that both the cytoplasm and the nucleus inside the cytoplasm contribute to the convergent lens effect due to their positive RI contrast (see Figure 1c,f), while the vacuole inside the cytoplasm acts as a divergent lens due to its negative RI contrast (see Figure 1f). In fact, the focal distance of a homogeneous sphere can be computed as[18]

$$f \approx \frac{1}{n_A} \frac{nd}{4\left(n - n_A\right)} \tag{1}$$

where d is the diameter of the sphere, n is its RI, and n_A is the RI of the surrounding ambience. Hence, for mostly convex objects such as the cellular compartments here considered, their positive/negative RI contrast $\Delta n = n - n_A$ is responsible for their positive/negative lens effect, respectively.

2.1. Characterization of the Negative Biolens' Effect Through a DH-Based Method

To characterize the behavior of the reconstructed cells as biolenses, we employ the Integral Beam Propagation Method (IBPM) to emulate the in-focus complex wavefront produced when an incident plane wave passes through the 3D spatial distribution of the cell's RIs. In fact, we consider a linear model to approximate the beam propagation, thus a quantitative phase map (QPM)[48] is given by the integration of the RI values along the optical z-axis,[49] i.e.,

$$QPM\ (x, y) = \frac{2\pi}{\lambda} \int_z \left[n\left(x, y, z\right) - n_0\right] dz \tag{2}$$

where $n(x, y, z)$ is the 3D RI spatial distribution, n_0 is the RI of the surrounding medium, and λ is the wavelength of the incident beam. The QPMs reprojected from the 3D RI tomograms in Figure 1a,d are respectively shown in **Figure 2**a,b, while the comparison with the corresponding experimental QPMs is reported in Figure S2a,c,f,h (Supporting Information), respectively. It is important to note that, even if QPMs are 2D images, they condense the whole cellular information. Indeed, in a 2D QPM, the 3D RI spatial distribution is coupled to the 3D cell's morphology. Moreover, biological cells are often defined as "phase objects" since they mainly change the phase of the incident light while leaving mostly unchanged its amplitude.[48] This can be seen in the amplitude maps displayed in Figure S2b,g (Supporting Information), corresponding to the QPMs of the iso-cell and hypo-cell in Figure S2a,f (Supporting Information), respectively, in which cells are almost transparent. Therefore, the vacuolar compartment can also be observed at the lowest phase values of the hypo-cell in Figure 2b, as well as the nucleus can be recognized at the highest phase values for both the iso-cell and hypo-cell in

Figure 2a,b. For this reason, the 2D QPM can be exploited to investigate the biolens' effect. It is worth underlining that one of the main advantages offered by DH is the possibility of numerically refocusing the recorded digital hologram. This is particularly important in the case of imaging flow cytometry experiments, where usually cells are not recorded exactly in their foci. At this aim, the complex wavefront is numerically propagated along the optical z-axis through the Angular Spectrum formula,[24] and an amplitude contrast metric is minimized in order to compute the in-focus z-position of each cell.[50] Then, in order to investigate the biolens' effect, starting from the in-focus z-position, we numerically propagate the complex wavefront along the positive and negative directions of the optical z-axis by considering in this case study a unitary amplitude due to the cell amplitude transparency shown in Figure S2b,g (Supporting Information). The in-focus z-position is considered as the origin of the reference system and is located approximately in the middle of the cell volume (i.e., 81 μm^3 for the iso-cell and 252 μm^3 for the hypo-cell). For each z-position, we compute the maximum value of the intensity of the propagated complex wavefront.[17] The max-intensity curves related to the iso-cell and the hypo-cell are reported in green at the bottom of Figure 2c,d, respectively.

To recognize the contributions of different cellular compartments, we have exploited the experimental tomograms in Figure 1 to generate various scenarios by isolating their main components. In particular, for both the iso-cell and hypo-cell, we have generated the cytoplasm tomogram, i.e., a tomogram having the same shell of the cell and a homogeneous RI value equal to the mean cell RI, immersed in the same experimental surrounding medium (see the corresponding QPMs in Figure S2d,i, Supporting Information, respectively). Then, for both the iso-cell and hypo-cell, we have generated the nucleus tomogram, i.e., a tomogram having the same shell of the segmented nucleus and a homogeneous RI value equal to the mean nucleus RI, immersed in a surrounding medium having as RI the mean value of the overall cell, except for the nucleus volume (see the corresponding QPMs in Figure S2e,j (Supporting Information). Finally, for the sole hypo-cell, we have generated the vacuole tomogram, i.e., a tomogram having the same shell of the segmented vacuole and a homogeneous RI value equal to the mean vacuole RI, immersed in a surrounding medium having as RI the mean value of the overall cell, except for the vacuole volume (see the corresponding QPM in Figure S2k, Supporting Information). Note that phase values are negative for the vacuole QPM, since the RI contrast between this compartment and the surrounding medium is negative. Hence, we have computed the max-intensity curves related to the cytoplasm (yellow), the nucleus (red), and the vacuole (blue), displayed at the bottom of Figure 2c,d. The different peaks inside the max-intensity curves of the overall cell (green) imply different focalizations of its equivalent biolens. To highlight this, we show at the top of Figure 2c,d the intensity profiles corresponding to the yellow lines in Figure 2a,b, respectively, which are the intensity values (ordinate axis) computed at each axial position (abscissa axis) along the sole yellow lines. In particular, by comparing the max-intensity curves of the overall cells with the max-intensity curves of the single compartments, it can be seen that the main peaks on the right are due to the cytoplasm' focalization, while the intermediate peak in the middle is due to the nucleus' focalization. Thus, as sketched in Figure 1b,c,e,f, both the overall cell and the sole nucleus act as positive convergent lenses, since they focus the incident light forward along the optical axis, as they have a positive RI contrast with respect to their surrounding medium.[18] Moreover, as the overall cytoplasm is bigger than the sole nucleus, its focal length is longer and its focalization is more intense. However, in the intensity profile and in the green max-intensity curve of Figure 2d, a virtual negative focalization can also be observed. The negative peak is also present inside the vacuole max-intensity curve, while it is missing in the max-intensity curve of the iso-cell in Figure 2c, in which the formation of a large vacuole has not occurred. Therefore, this means that the large and roundish vacuole inside the yeast cell can focus the incident light backward along the optical axis, thus acting as a negative divergent lens, as sketched in Figure 1e,f. This can be explained by the negative RI contrast between the vacuole and its surrounding medium (i.e., both the cytoplasm and the nucleus),[18] already observed in the negative phase values in Figure S2k (Supporting Information). In summary, starting from the experimental DH imaging of yeast cells, the max-intensity curve can be created by using the Angular Spectrum to numerically emulate the virtual light propagation along the negative optical axis,[24] thus obtaining the virtual negative focalization displayed in Figure 2d. In this way, the focal properties of such divergent optical elements can be measured. Hence, the DH-based method allows an easy and fast numerical characterization of the positive/negative focal properties of cell biolenses, which replaces complex and time-consuming experimental characterizations, above all in the case of divergent biolenses.

2.2. Assessment of the Negative Biolens' Effect Through Zemax OpticStudio

The characterization of the positive-negative focal properties of a yeast cell bio-engineered as an optical system of biolenses has been demonstrated so far through the DH-based method in Matlab R2022a. However, a commercial software specific to the optical design, i.e., Zemax OpticStudio, has also been employed to confirm and strengthen the attained results. At this aim, we have considered the cytoplasm tomogram for both the iso-cell and hypo-cell. For both of them, the Huygens Point Spread Functions (PSFs) have been computed along the optical z-axis, and the maximum value has been calculated. Since the cell size is fewer times larger than the light wavelength, the diffraction effects play an important role in the shape, intensity, and size of the images along the z-axis. The calculation of the Huygens PSF in Zemax OpticStudio is done by converting each ray on the Spot Diagram into a small plane wave. The total irradiance at any point on the image surface may be determined by coherently summing all the plane waves represented by all the traced rays. Details about these simulations are reported in the Supplemental Document. The plots of the maxima of the PSFs as a function of the z-position (namely, max-PSF curves) are reported in **Figure** 3a, normalized to the maximum value of the max-PSF curve about the iso-cell. In both cases, the max-PSF curve exhibits a peak in the positive z-axis due to the real positive focalization of the whole cell, while the negative values are close to 0. Furthermore, an additional scenario has been generated from the hypo-cell, i.e., the cytoplasm/vacuole tomogram, that is the cytoplasm tomogram

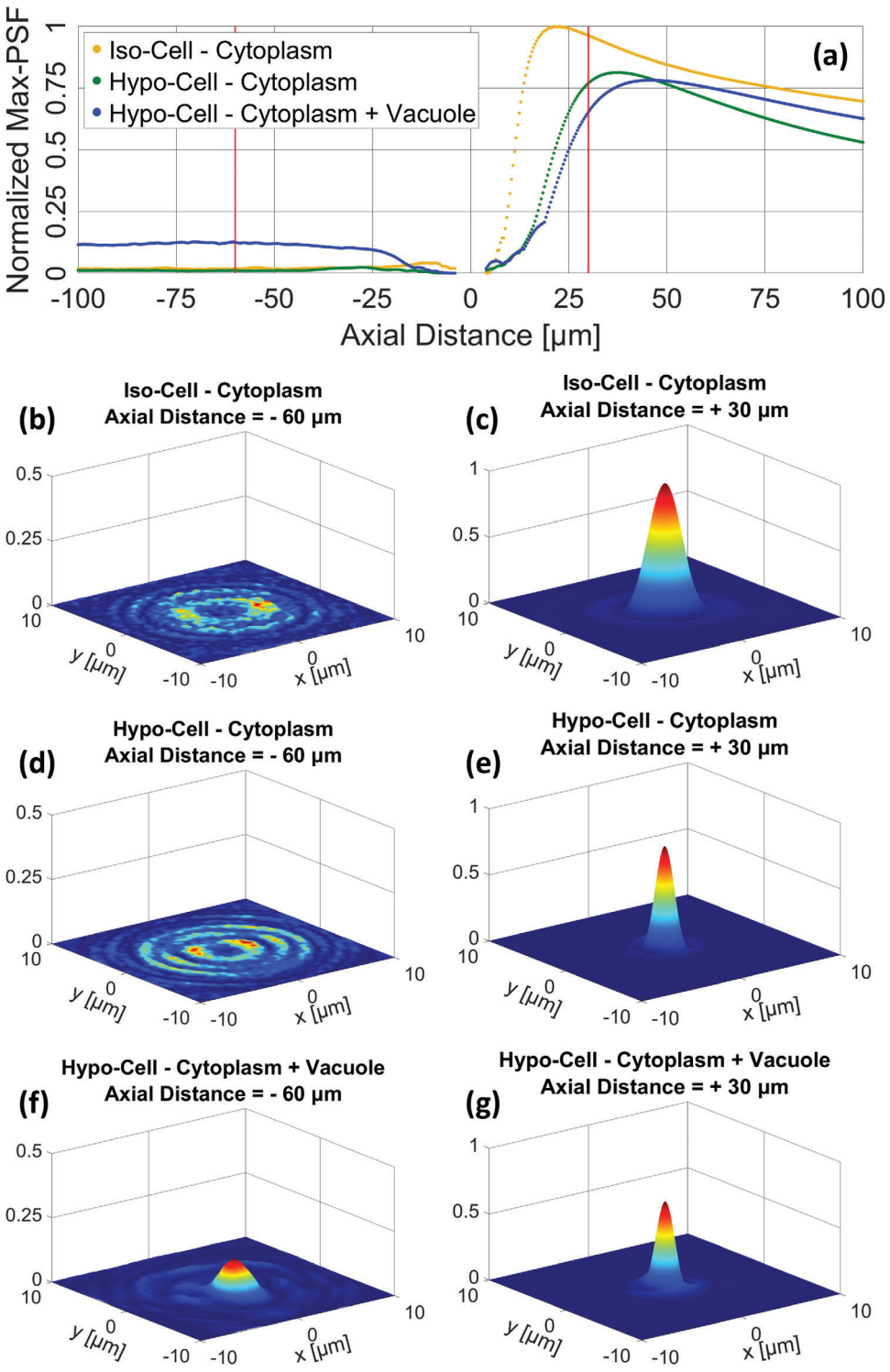

Figure 3. Optical properties of a yeast iso-cell and a yeast hypo-cell obtained through simulations in Zemax OpticStudio. a) Normalized max-PSF curves of the sole cytoplasm about the iso-cell (yellow) and the hypo-cell (green), and the cytoplasm/vacuole of the hypo-cell (blue). b,d,f) Normalized Huygens PSF about the cytoplasm tomograms of the iso-cell and hypo-cell and the cytoplasm/vacuole tomogram of the hypo-cell, respectively, at -60 µm. c,e,g) Normalized Huygens PSF about the cytoplasm tomograms of the iso-cell and hypo-cell and the cytoplasm/vacuole tomogram of the hypo-cell, respectively, at +30 µm.

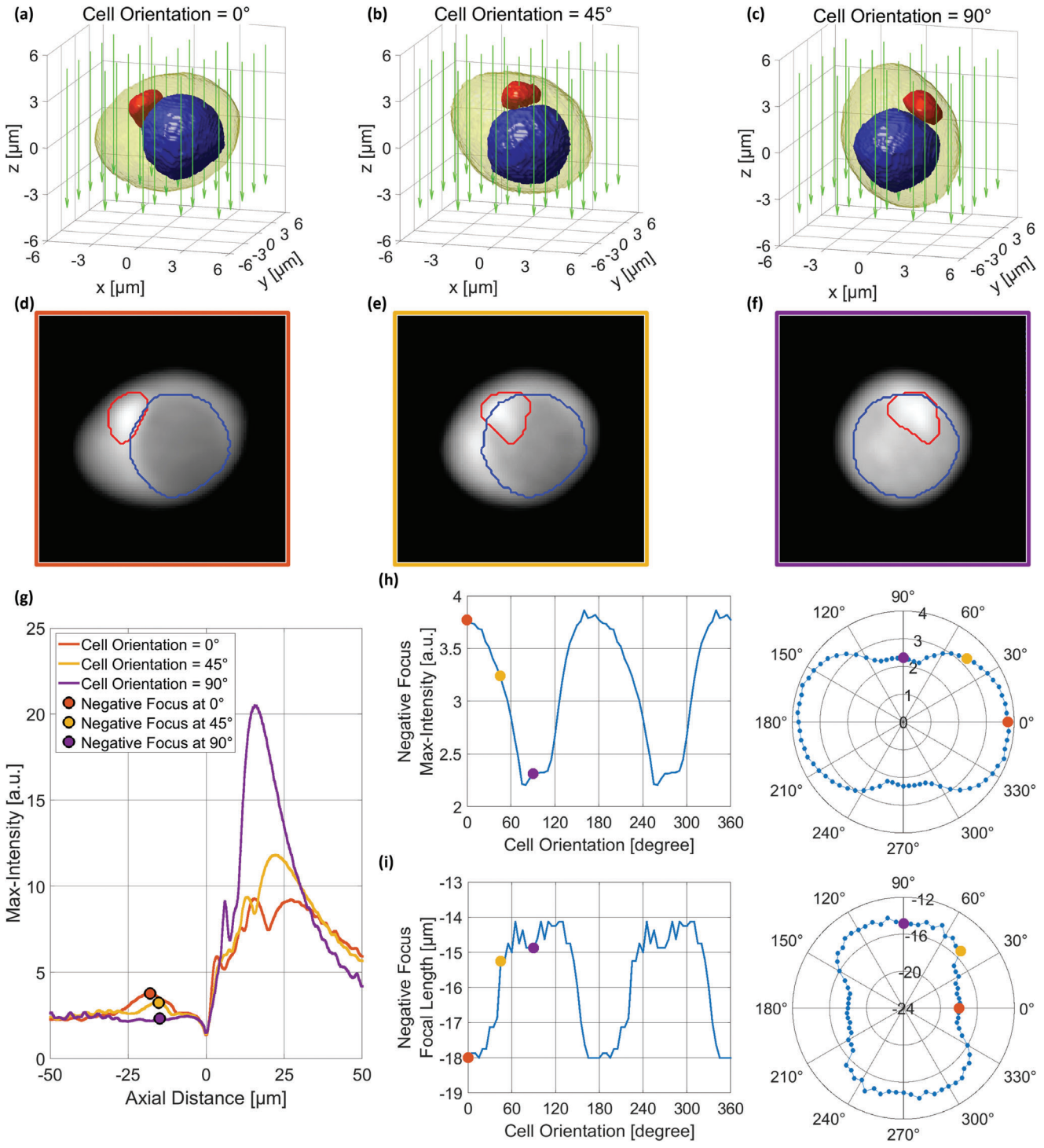

Figure 4. Focalization of a yeast hypo-cell at different cell orientations with respect to the incident beam direction (see Video S2, Supporting Information, with the whole cell rotation). a–c) Isolevels representation of the cytoplasm (yellow) along with the vacuole (blue) and the nucleus (red) at respectively 0°, 45°, and 90° of rotation around the y-axis, and d–f) corresponding QPMs, respectively, reprojected through the IBPM by keeping fixed the illumination beam direction along the z-axis (green arrows in (a-c)). g) Max-intensity curves computed from the QPMs in (d-f) at 0°, 45°, and 90°, respectively, in which the corresponding virtual negative focal positions are highlighted (colored dots). h) Max-intensity value in the virtual negative focus at different cell orientations in cartesian (left) and polar (right) coordinates. i) Negative focal length at different cell orientations in cartesian (left) and polar (right) coordinates.

having the mean RI of the measured vacuole inside the vacuolar shell (see Figure S3c, Supporting Information). The corresponding max-PSF curve, normalized to the maximum value of the max-PSF curve about the iso-cell, in addition to the positive peak, shows higher values at the negative z-distances due to the presence of the vacuolar structure and its virtual negative focalization. The ratio between the average value at negative and positive axial distances has been computed to quantify it. This ratio is 0.03 for the cytoplasm tomogram in both the iso-cell and hypo-cell, while it raises to 0.23 for the cytoplasm/vacuole tomogram in the hypo-cell, thus confirming that the hypo-cell is also showing a virtual negative focalization beyond the main real positive focalization.

But, in addition to the validation of the DH-based biolens characterization, simulations in Zemax OpticStudio provide a powerful tool to compute the Huygens PSF of the cell, considered as an optical system able to focus the incident light beam in the positive and/or negative directions. For example, the Huygens PSFs are displayed in Figure 3b,d,f at -60 µm and in Figure 3c,e,g at +30 µm, respectively, for the cytoplasm tomograms of the iso-cell and hypo-cell and the cytoplasm/vacuole tomogram of the hypo-cell. As discussed before, in all three cases, the Huygens PSFs have a high positive peak (see Figure 3c,e,g), while the sole cytoplasm/vacuole tomogram exhibits a pronounced negative peak (see Figure 3f).

2.3. Positive-Negative Focal Properties of the Optical System of Biolenses

In summary, if the cytoplasm and the nucleus are individually considered, they behave as positive convergent lenses, while the vacuole is equivalent to a negative divergent lens. For this reason, the overall cell can be considered an optical system of biolenses with positive-negative focal properties, which are expected to change according to its orientation with respect to the incident beam. By exploiting the DH-based method and the possibility offered by TPIFC of reconstructing a cell in suspension, in **Figure** 4a–c we have considered three different orientations of the hypo-cell around the y-axis, i.e., 0°, 45°, and 90°, respectively, while we have reprojected the corresponding QPMs in Figure 4d–f, respectively. In particular, as reported in Figure 4a–c, the cell orientation corresponds to the angle formed by the cell's major axis with respect to the XY-plane, and it is positive for clockwise rotations around the y-axis.

For each QPM, we have computed the max-intensity curves reported in Figure 4g. It can be observed that, passing from 0° to 90°, the max-intensity value in the virtual negative focus (i.e., the value of the marked local peak) gradually decreases, as well as the negative focal length (i.e., the position of the marked local peak). On the contrary, the positive peak gradually increases. In fact, by defining the peak ratio as the ratio between the max-intensity of the negative and the positive peaks, it is 0.41 at 0°, 0.27 at 45°, and 0.11 at 90°. This means that, while the optical system made of the overall cell at 0° is able to focus the incident beam toward both the positive and the negative directions, at 90° it mainly acts as a positive lens. This is due to the relative positions among the cytoplasm, the nucleus, and the vacuole. In fact, at 0°, the nucleus and the vacuole are not overlapped with respect to the beam direction and, in addition, the light passes through a small portion of the cytoplasm, as the cell is exposing its short side to the wavefront (see Figure 4a,d). Thus, this is the case where the negative biolens effect is more effective. Instead, this effect fades at 45°, where the nucleus is overlapped to the vacuole with respect to the incident beam direction (see Figure 4b,e). Finally, the negative biolens effect disappears at 90°, since the nucleus is still overlapped to the vacuole, but, in addition, the incident light must cross the long side of the cell, thus mostly contributing to the positive biolens effect (see Figure 4c,f).

Table 1. Focal features of the yeast hypo-cell related to its rotation around the sole y-axis (see Figure 4).

Focal Feature	Single Cell
Minimum Negative Focal Length [µm]	14.1
Maximum Negative Focal Length [µm]	18
Minimum Positive Focal Length [µm]	15.5
Maximum Positive Focal Length [µm]	27.3
Minimum Negative Focal Max-Intensity [a.u.]	2.2
Maximum Negative Focal Max-Intensity [a.u.]	3.9
Minimum Positive Focal Max-Intensity [a.u.]	9.2
Maximum Positive Focal Max-Intensity [a.u.]	20.6

To better visualize the discussed dependence between the focal properties of the cell and its orientation with respect to the incident beam, in Figure 4e we report the max-intensity values in the virtual negative focus at different cell orientations (both in cartesian and in polar coordinates), and in Figure 4f we display the negative focal length at different cell orientations (both in cartesian and in polar coordinates). In both cases, a sinusoidal trend of the cell focal properties is observed, which can be expected since the interval of cell rotations between 0° and 90° includes all the possible relative positions among the cytoplasm, the nucleus, and the vacuole with respect to the incident beam. The focal features of both the negative and the positive focus are summarized in **Table 1**, which refers to the rotation of the cell around the sole y-axis. Of course, in principle, the TPIFC technique allows characterizing the focal properties of the cellular biolens along any direction in 3D space, thus simulating, for example, an optical manipulation of the cell by means of optical tweezers.[51]

2.4. An example of Complex Optical System of Positive-negative Biolenses

Yeast cells are often used as biological models for the eukaryotic cell since they easily and quickly duplicate (the division time takes an average of 90 min).[45] The division process of yeast cells is defined as "budding" since the daughter cell buds off the mother cell and then it detaches, thus forming a new yeast cell.[45,52] An example of a budding yeast cell after the vacuolar alteration is shown in **Figure 5**a, in which the smaller daughter cell is placed to the left of the bigger mother cell, thus leading to the reprojected QPM in Figure 5b. It can be seen that the whole cell in Figure 5a,b is made of two cells side by side in which the nucleus and the vacuole are not overlapped with respect to the optical axis, as for the

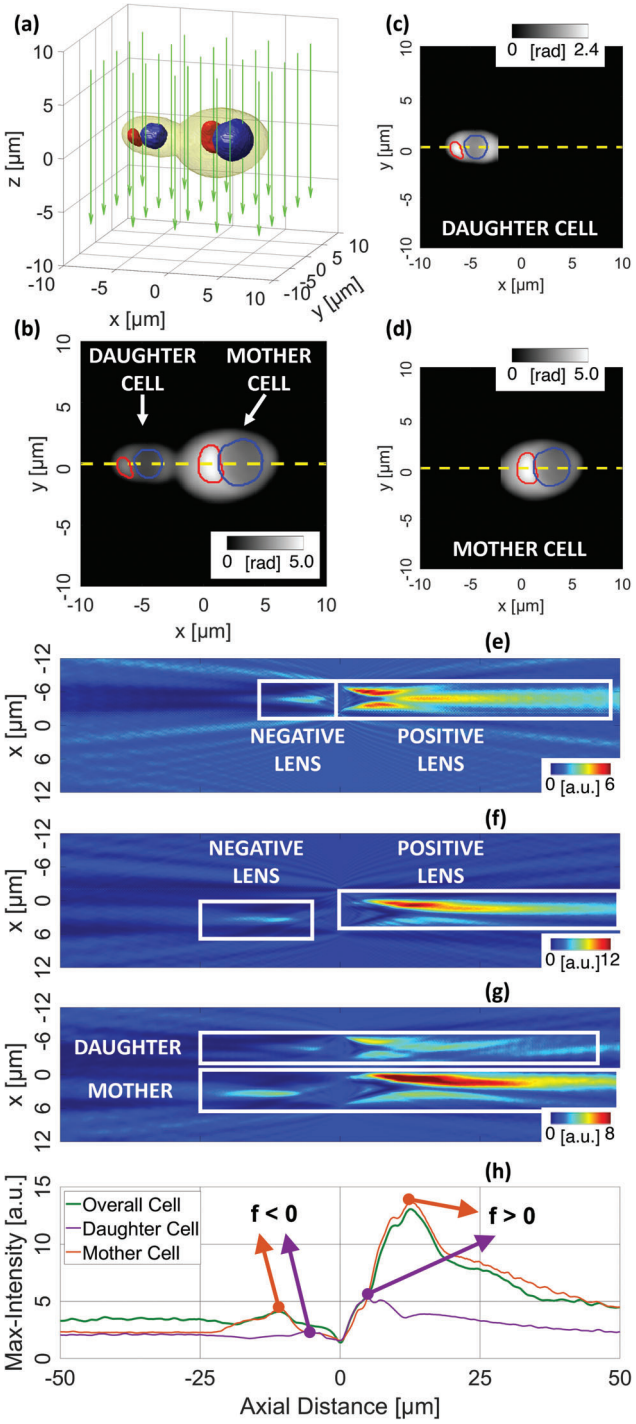

Figure 5. Focalization of a budding yeast hypo-cell. a) Isolevels representation of the whole cell (yellow) along with its vacuoles (blue) and nuclei (red), and b) corresponding QPM reprojected through the IBPM along the z-axis (green arrows in (a)). c,d) Reprojected QPMs of respectively the daughter and mother cells cropped on the left and the right side of the QPM in (b). e–g) Intensity profile made of the intensity values computed for each axial distance along the yellow line in (b-d), respectively. In (g), the intensity values are saturated to make visible the daughter cell's focalization. h) Max-intensity curve of the whole cell (green), the daughter cell (violet), and the mother cell (orange). Arrows indicate focal planes.

Table 2. Focal features of the budding yeast hypo-cell at 0° around the y-axis (see Figure 5).

Focal Feature	Daughter Cell	Mother Cell
Negative Focal Length [µm]	5.8	10.9
Positive Focal Length [µm]	4.9	12.5
Negative Focal Max-Intensity [a.u.]	2.4	4.3
Positive Focal Max-Intensity [a.u.]	5.3	13.6

case in Figure 4a,d. This is better shown in Figure 5c,d, in which the reprojected QPM of the whole cell in Figure 5b has been separated in the contributions of the daughter cell and the mother cell, respectively. As already demonstrated, in such conditions, the two yeast cells exhibit focal properties typical of both convergent and divergent lenses, as also visible in the intensity profiles in Figure 5e,f corresponding to the yellow lines in Figure 5c,d, respectively.

When considering the whole yeast cell in Figure 5b , as the incident beam passes separately through the two cells and not sequentially, their biolens' properties remain unchanged, as shown in the intensity profile of Figure 5g. Of course, as also reported in the more informative max-intensity curve of Figure 5h, the daughter cell is smaller than the mother one, thus its positive and negative focal lengths are shorter as well as the max-intensity values in the positive and negative focal planes are lower. Therefore, a budding yeast cell can act as a complex optical system made of two optical systems of biolenses having different focal properties, each of which in turn behaves simultaneously as an equivalent positive and negative lens, due to the reshaping of a large and roundish vacuole (see the quantitative focal features summarized in **Table 2**).

3. Conclusion

We have shown that, starting from a live biological cell acting as a positive optical lens, an optical system of biolenses can be bioengineered to induce positive as well as negative lensing effects. This process was achieved by altering the intracellular content instead of morphing the cell shape. In particular, we reshaped the intracellular vacuoles inside the cytoplasm of yeast cells by inducing hypotonic conditions in the surrounding buffer, thus leading to the formation of one single large and roundish vacuole. Because of a lower RI with respect to the embedding cytoplasm, the reshaped vacuole behaves as a negative optical biolens. Therefore, in the morphed yeast cell, a virtual negative focalization is added to the main real positive one. The investigation was performed through a phase-contrast holo-tomographic flow-cytometry technique at the single-cell level, namely TPIFC. The in-flow tomographic tool allowed obtaining the 3D RI distribution of the cells in suspension conditions, which were exploited to isolate the contributions of several intracellular components to the focal properties of the overall optical system of biolenses, i.e., the cell. Moreover, we employed TPIFC to demonstrate that the positive-negative focal properties of this optical system of biolenses change according to its orientation with respect to the incident light. In particular, there are some orientations where the virtual negative focalization is more evident than others. The

characterization of the focal properties of yeast cells recorded by TPIFC was performed by means of a DH-based model. Furthermore, verification of the focal properties of such optical systems of biolenses was also performed through a numerical study by Zemax OpticStudio. Remarkably, the output of numerical simulations in Zemax OpticStudio were in good agreement with the well-established DH-based characterization of focal properties related to the experimental yeast cells. Finally, a budding yeast cell was analyzed as an even more complex optical system able to perform several positive-negative focalizations of the incident light.

The attained results represent a significant step forward along the route of generating biological lenses with programmed optical functions. Of course, future works are needed to overcome current limitations. For example, one limitation is linked to the hypotonic conditions necessary to trigger the vacuole property as negative biolens. The formation of the large roundish vacuole needs just a few minutes under hypotonic conditions, which can easily be generated by placing yeast cells in water. Although yeast cells can survive in water due to their quick adaptation to hypotonic shocks,[53] without nutrients, cells can be analysed only for a limited time which should not exceed a few hours of incubation to avoid inducing significant morphological alterations of the intracellular organelle as well as the entire cell. To further improve this time period for exploiting yeast vacuoles as negative biolenses, in the future, this property can be investigated on purified vacuoles. Indeed, once purified, vacuoles can preserve their biochemical properties, and their morphology does not suffer from the lack of nutrients.[54,55] At the same time, to move toward the scaling up of this technology for real-world use, future studies will be dedicated to fine-tune the bio-engineering protocols for the creation of a large roundish vacuole as negative lens in order to have a better control on its focal properties.

In summary, in this study we expanded the scope of the biolens paradigm by focusing not only on the overall morphology of the cell but also on its specific inner structures. This innovative approach opens new avenues for bio-engineering live cells and customizing their optical properties, broadening the horizons of what can be achieved in this field. The goals of tailoring living samples as micro-lenses or micro-lenses array may be grouped in two main classes: (i) exploiting cells to obtain optical functionalities at the microscale as sub-diffraction imaging or optical tweezers; (ii) diagnostic purposes. In case of the first-class applications, the driving reasons are the intrinsic biocompatibility of the optical component that is necessary in some imaging modalities as in endoscopy and the complete skipping of multi-step fabrication processes. All the possible applications will be subject of future studies, which will also entail analyzing different lighting conditions and wavelengths to grasp crucial lensing parameters like focal length and numerical aperture. Instead, in the context of the first-class applications, harnessing the bio-lensing properties for diagnostics presents numerous advantages, primarily due to the ability to achieve comprehensive label-free fingerprinting of biological samples. This stands in stark contrast to traditional bio-chemical and genetic analyses. To enlarge the spectrum of biomedical applications, it would be useful to study the lens property of vacuoles also in mammals, since their detection could profoundly impact clinical diagnosis.

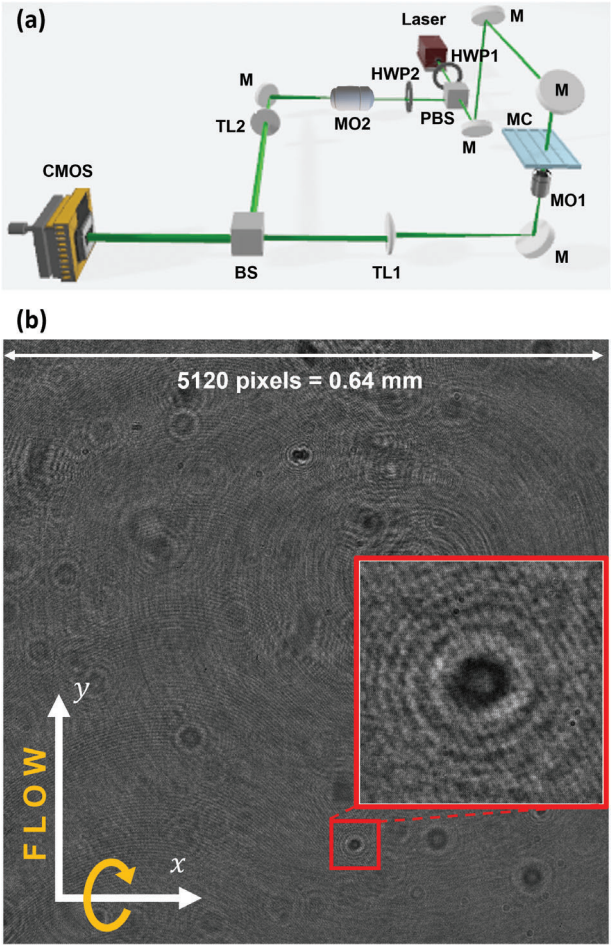

Figure 6. TPIFC experimental setup. a) Sketch of the opto-fluidic recording system. HWP1, HWP2 – Half-Wave Plates; PBS – Polarizing Beam Splitter; TL1, TL2 – Tube Lenses; M – Mirror; MO1, MO2 – Microscope Objectives; MC – Microfluidic Channel; BS – Beam Splitter; CMOS – Camera. b) Recorded digital hologram, with the cell's diffraction visible in the holographic ROI highlighted in red.

4. Experimental Section

Sample Preparation: Yeast cells were grown at 30 °C on YPD (yeast extract, peptone, dextrose 2%) agar-plate up to the colony's formation. After that, the individual colony was picked up and grown in liquid YPD for overnight incubation at 30 °C with agitation. The day after, cells were diluted in a new tube in YPD up to 0.02OD (optical density) and incubated for an additional 24 h before processing. 0.5OD of cells were imaged before and after 10 min of incubation at 30 °C in water (hypotonic conditions) or in PBS (phosphate buffer for isotonic conditions).

TPIFC Experiments: The TPIFC experimental setup comprises two modules, i.e., an optical module and a microfluidic module, as sketched in **Figure 6**a.[22] The optical module was a DH microscope based on an off-axis Mach-Zehnder optical interferometer. The light beam created by a solid-state continuous wave laser source (Laser Quantum Torus 532 – λ = 532 nm) was split into a reference and an object beam by a polarizing beam splitter (PBS). The splitting ratio between the two beams was adjusted by two half-wave plates (HWP1 and HWP2) located in front of and behind the PBS. After passing through the biological sample, the object beam was collected by a microscope objective (MO1) and sent to a tube lens (TL1). Meanwhile, the reference beam was collected by a MO2 and a TL2. The interference pattern produced by the object and reference

beams within the beam splitter cube (BS) propagates up to the CMOS recording camera (Genie Nano-CXP Camera, 5120 × 5120 pixels, $\Delta x = \Delta y = 4.5$ µm pixel size), thus resulting in the recorded digital hologram (see the example in Figure 6b, measuring 640 × 640 μm^2. The microfluidic module was instead made of a low-pressure pump module (Cetoni NEMESYS 290 N) that generates a laminar flow at 75 nL/s within a commercial microfluidic channel (Microfluidic – ChipShop 10 000 107, 200 μm × 1000 μm cross-section), where the biological sample made of single cells could flow and rotate. In particular, cells flow along to the y-axis, rotate around the x-axis, and are recorded along the optical z-axis, according to the reference system displayed in Figure 6b.

Thanks to the TPIFC experimental system, hundreds of holograms were recorded for each flowing/rotating cell. From the recorded holographic video sequence, a subsequence of QPMs containing its roto-translation was computed for each cell.[23] At this aim, as shown in Figure 6b, a region of interest (ROI) was selected within each full hologram around each cell.

The holographic ROI was demodulated through a band-pass filter in the Fourier domain to extract the real diffraction order, thanks to the DH off-axis configuration.[24] The DH microscopy allows recording cells out-of-focus in any position along the optical z-axis, since the real in-focus distance could be numerically computed by means of a refocusing method based on the Tamura Coefficient.[50] The out-of-focus demodulated complex field was then numerically propagated at the computed in-focus z-position through the Angular Spectrum formula.[24] The same operations were carried out over a reference hologram, i.e., a hologram recorded without any cell inside, in order to remove residual phase aberrations by subtracting the argument of the in-focus reference complex field from the argument of the in-focus cell complex field.[56] Finally, the resulting phase map was denoised by the 2D windowed Fourier transform filtering[57] and unwrapped by the PUMA algorithm,[58] thus obtaining the QPMs as those displayed in Figure 2a,b. For each cell, the sequence of QPMs was centered around its centroids, and the corresponding unknown rolling angles were estimated from the tracking positions.[59] Finally, the sequence of centered QPMs and corresponding estimated rolling angles were employed to reconstruct the 3D RI tomogram through the Filtered Back Projection algorithm,[60] as shown in Figure 1a,d.

Supporting Information

Supporting Information is available from the Wiley Online Library or from the author.

Acknowledgements

This work was supported by a project PRIN 2022 – Label-free cytoplasmic vacUoles pheNotyping plAykit (LUNA) Prot. 960, 30th June 2023 – funded by the Italian Ministry of University & Research in the framework of the European Union program Next Generation EU (Project CUP: B53D23002490006). This work was supported by project POR CIRO (Campania Imaging for Research in Oncology) funded by Regione Campania (Italy). This work was supported by project BIOLENTI – Sistemi ottici basati su Biolenti in diversi ambiti di ricerca e applicazioni industriali (SOBRI) – of the National Research Council of Italy (Project CUP: B53C22005870005).

Conflict of Interest

The authors declare no conflict of interest.

Data Availability Statement

The data that support the findings of this study are available from the corresponding author upon reasonable request.

Keywords

biolens, digital holography, phase-contrast tomography, quantitative phase imaging, single-cell analysis

Received: January 18, 2024
Revised: April 3, 2024
Published online:

[1] M. C. Gather, S. H. Yun, *Nat. Photonics* **2011**, *5*, 406.
[2] M. J. Booth, *Light: Sci. Appl.* **2014**, *3*, e165.
[3] L. Miccio, P. Memmolo, F. Merola, P. A. Netti, P. Ferraro, *Nat. Commun.* **2015**, *6*, 6502.
[4] L. Miccio, P. Memmolo, F. Merola, M. Mugnano, P. Ferraro, *J. Phys. Photonics* **2020**, *3*, 012003.
[5] F. Merola, Á. Barroso, L. Miccio, P. Memmolo, M. Mugnano, P. Ferraro, C. Denz, *Cytometry A* **2017**, *91*, 527.
[6] P. Memmolo, D. Pirone, D. G. Sirico, L. Miccio, V. Bianco, A. B. Ayoub, P. Ferraro, *Intell. Comput.* **2023**, *2*, 0010.
[7] Y. Li, X. Liu, B. Li, *Light: Sci. Appl.* **2019**, *8*, 61.
[8] S. Y. Cho, X. Gong, V. B. Koman, M. Kuehne, S. J. Moon, M. Son, T. T. S. Lew, P. Gordiichuk, X. Jin, H. D. Sikes, M. S. Strano, *Nat. Commun.* **2011**, *12*, 3079.
[9] S. Y. Cho, V. B. Koman, X. Gong, S. J. Moon, P. Gordiichuk, M. S. Strano, *ACS Nano* **2011**, *15*, 13683.
[10] S. Jiang, C. Guo, T. Wang, J. Liu, P. Song, T. Zhang, R. Wang, B. Feng, G. Zheng, *ACS Sens.* **2022**, *7*, 1058.
[11] R. Gautam, Y. Xiang, J. Lamstein, Y. Liang, A. Bezryadina, G. Liang, T. Hansson, B. Wetzel, D. Preece, A. White, M. Silverman, S. Kazarian, J. Xu, R. Morandotti, Z. Chen, *Light: Sci. Appl.* **2019**, *8*, 31.
[12] Y. X. Ren, J. Lamstein, C. Zhang, C. Conti, D. N. Christodoulides, Z. Chen, *Photonics Res.* **2023**, *11*, 1838.
[13] P. Memmolo, L. Miccio, F. Merola, P. Ferraro, *JPhys Photonics* **2020**, *2*, 035005.
[14] Y. Li, X. Liu, X. Yang, H. Lei, Y. Zhang, B. Li, *ACS Nano* **2017**, *11*, 10672.
[15] X. Liu, Y. Li, X. Xu, Y. Zhang, B. Li, *ACS Appl Bio Mater* **2019**, *2*, 2889.
[16] X. Chen, T. Wu, Z. Gong, J. Guo, X. Liu, Y. Zhang, Y. Li, P. Ferraro, B. Li, *Light: Sci. Appl.* **2021**, *10*, 242.
[17] D. Pirone, D. G. Sirico, M. Mugnano, D. Del Giudice, I. Kurelac, B. Cavina, P. Memmolo, L. Miccio, P. Ferraro, *Biomed. Opt. Express* **2022**, *13*, 5585.
[18] J. Běhal, D. Pirone, D. Sirico, V. Bianco, M. Mugnano, D. Del Giudice, B. Cavina, I. Kurelac, P. Memmolo, L. Miccio, P. Ferraro, *Cytometry A* **2023**, *103*, 251.
[19] V. Bianco, M. D'Agostino, D. Pirone, G. Giugliano, N. Mosca, M. Di Summa, G. Scerra, P. Memmolo, L. Miccio, T. Russo, E. Stella, P. Ferraro, *Small Methods* **2023**, *7*, 2300447.
[20] M. Lee, M. Kunzi, G. Neurohr, S. S. Lee, Y. Park, *Biomed. Opt. Express* **2023**, *14*, 4567.
[21] M. Habaza, B. Gilboa, Y. Roichman, N. T. Shaked, *Opt. Lett.* **2015**, *40*, 1881.
[22] D. Pirone, J. Lim, F. Merola, L. Miccio, M. Mugnano, V. Bianco, F. Cimmino, F. Visconte, A. Montella, M. Capasso, A. Iolascon, P. Memmolo, D. Psaltis, P. Ferraro, *Nat. Photonics* **2022**, *16*, 851.
[23] D. Pirone, D. Sirico, L. Miccio, V. Bianco, M. Mugnano, P. Ferraro, P. Memmolo, *Lab Chip* **2022**, *22*, 793.
[24] M. K. Kim, *SPIE Rev.* **2010**, *1*, 018005.
[25] C. Jiang, H. Yue, B. Yan, T. Dong, X. Cui, P. Chen, Z. Wang, *Biomed. Opt. Express* **2023**, *12*, 7113.
[26] H. Bian, Y. Wei, Q. Yang, F. Chen, F. Zhang, G. Du, J. Yong, X. Hou, *Appl. Phys. Lett.* **2016**, *109*, 221109.

[27] S. Ghislanzoni, J. W. Kang, A. Bresci, A. Masella, K. J. Kobayashi-Kirschvink, D. Polli, I. Bongarzone, P. T. So, *Biosensors* **2023**, *13*, 973.
[28] G. Scerra, V. De Pasquale, L. M. Pavone, M. G. Caporaso, A. Mayer, M. Renna, M. D'Agostino, *iScience* **2021**, *24*, 102707.
[29] G. Scerra, M. G. Caporaso, M. Renna, M. D'Agostino, *STAR Protoc.* **2021**, *2*, 100916.
[30] A. R. Marques, P. Saftig, *J. Cell Sci.* **2019**, *132*, jcs221739.
[31] M. R. Ambrosio, P. P. Piccaluga, M. Ponzoni, B. J. Rocca, V. Malagnino, M. Onorati, G. De Falco, V. Calbi, M. Ogwang, K. N. Naresh, S. A. Pileri, C. Doglioni, L. Leoncini, S. Lazzi, *PLoS One* **2012**, *7*, e44315.
[32] D. T. Lynch, K. Foucar, *Am. J. Hematol.* **2016**, *127*, 3292.
[33] O. Ballo, J. Stratmann, H. Serve, B. Steffen, F. Finkelmeier, C. Brandts, *PLoS One* **2019**, *14*, e0223013.
[34] J. Song, B. Shang, Y. Pei, M. Shi, X. Niu, L. Dou, E. K. Drokow, F. Xu, Y. Bai, K. Sun, *Leuk. Res.* **2021**, *109*, 106638.
[35] Y. Zhao, E. Wang, *Am. J. Med. Sci.* **2021**, *362*, e27.
[36] A. V. Shubin, I. V. Demidyuk, N. A. Lunina, A. A. Komissarov, M. P. Roschina, O. G. Leonova, S. V. Kostrov, *BMC Cell Biol.* **2015**, *16*, 4.
[37] R. D. Satria, T. W. Huang, M. K. Jhan, T. J. Shen, P. C. Tseng, Y. T. Wang, Z. Y. Yang, C. H. Hsing, C. F. Lin, *J. Immunol. Res.* **2021**, *2021*, 6654617.
[38] B. Monel, A. A. Compton, T. Bruel, S. Amraoui, J. Burlaud-Gaillard, N. Roy, F. Guivel-Benhassine, F. Porrot, P. Génin, L. Meertens, L. Sinigaglia, N. Jouvenet, R. Weil, N. Casartelli, C. Demangel, E. Simon-Lorière, A. Moris, P. Roingeard, A. Amara, O. Schwartz, *EMBO J.* **2017**, *36*, 1653.
[39] A. Singh, N. Sood, V. Narang, A. Goyal, *BMJ Case Rep.* **2020**, *13*, e236117.
[40] A. O. Wong, M. Marthi, Z. I. Mendel, B. Gregorka, M. S. Swanson, J. A. Swanson, *Mol. Biol. Cell* **2018**, *29*, 657.
[41] R. J. Davidson, J. L. McPhie, *J. Clin. Pathol.* **1980**, *33*, 1193.
[42] T. Aki, A. Nara, K. Uemura, *Cell Biol. Toxicol.* **2012**, *28*, 125.
[43] X. Zhai, Y. El Hiani, *Cancers* **2020**, *12*, 3669.
[44] X. Wang, H. Zhang, X. Chen, *Cancer Drug Resist.* **2019**, *2*, 141.
[45] A. A. Duina, M. E. Miller, J. B. Keeney, *Genetics* **2014**, *197*, 33.
[46] S. V. Scott, D. J. Klionsky, *Curr. Opin. Cell Biol.* **1998**, *10*, 523.
[47] S. C. Li, P. M. Kane, *Biochim. Biophys. Acta, Mol. Cell Res.* **2009**, *1793*, 650.
[48] Y. Park, C. Depeursinge, G. Popescu, *Nat. Photonics* **2018**, *12*, 578.
[49] D. Jin, R. Zhou, Z. Yaqoob, P. T. So, *J. Opt. Soc. Am. B* **2017**, *34*, B64.
[50] P. Memmolo, C. Distante, M. Paturzo, A. Finizio, P. Ferraro, B. Javidi, *Opt. Lett.* **2011**, *36*, 1945.
[51] H. Zhang, K. K. Liu, *J. R Soc Interface.* **2008**, *5*, 671.
[52] M. B. Mayhew, E. S. Iversen, A. J. Hartemink, *J. R. Soc. Interface* **2017**, *14*, 20160993.
[53] S. Hohmann, *Microbiol. Mol. Biol. Rev.* **2002**, *66*, 300.
[54] M. D'Agostino, H. J. Risselada, A. Lürick, C. Ungermann, A. Mayer, *Nature* **2017**, *551*, 634.
[55] M. D'Agostino, H. J. Risselada, A. Mayer, *EMBO Rep.* **2016**, *17*, 1590.
[56] C. Trujillo, R. Castañeda, P. Piedrahita-Quintero, J. Garcia-Sucerquia, *Appl. Opt.* **2016**, *55*, 10299.
[57] Q. Kemao, *Appl. Opt.* **2004**, *43*, 2695.
[58] J. M. Bioucas-Dias, G. Valadao, *IEEE Trans Image Process* **2007**, *16*, 698.
[59] D. Pirone, P. Memmolo, F. Merola, L. Miccio, M. Mugnano, A. Capozzoli, C. Curcio, A. Liseno, P. Ferraro, *Appl. Opt.* **2021**, *60*, A277.
[60] A. C. Kak, M. Slaney, *Principles Of Computerized Tomographic Imaging*, Society for Industrial and Applied Mathematics, Philadelphia, USA **2001**.